CHEMISTRY OF MATERIALS

pubs.acs.org/cm

Article

Nonlinear Conductive Behavior of 2D-Selenido Stannates

Zhou Wu, Hongrong Hu, Bastian Weinert, Jasmin Aghassi-Hagmann, and Stefanie Dehnen*

Cite This: https://doi.org/10.1021/acs.chemmater.6c01405

Read Online

ACCESS | Metrics & More | Article Recommendations | Supporting Information

ABSTRACT: Chalcogenido metalates have long been regarded as cluster-based semiconductors, yet their conductive nature has not been studied in detail, although such compounds do bear potential for use in electronics. Herein, we introduce four new compounds, $(HDMMP)_2[Sn_3Se_7]\cdot(HDMMP)_2[Sn_2Se_6]_{0.5}$ (**1**), $(C_3C_1Im)_3(HDMMP)[Sn_3Se_7]_2$ (**2**), and their Cs^+-exchanged derivatives, $\mathbf{1}^{Cs}$ and $\mathbf{2}^{Cs}$ (HDMMP = protonated 2,6-dimethylmorpholine; C_3C_1Im = 1-propyl-3-methyl-imidazolium), all of which are based on 2D-$\{[Sn_3Se_7]^{2-}\}$ anionic substructures. Detailed current−voltage measurements on single crystals of **1** and **2** as well as their ion-exchanged derivatives were undertaken that indicated complex nonlinear and highly structure-dependent conductive properties. For **1**, the studies demonstrate that intercalation of molecular 0D-$[Sn_2Se_6]^{4-}$ units with higher negative charge density as compared to the 2D-$\{[Sn_3Se_7]^{2-}\}$ networks creates open circuits that lead to nonconductive characteristics. In contrast, the $I-V$ measurements carried out on **2** suggest a combination of electrical and ionic conductivity along horizontal and vertical directions of this compound based exclusively on the 2D-$\{[Sn_3Se_7]^{2-}\}$ substructures. Cation exchange in **1** and **2** with Cs^+, which in the case of compound **1** is accompanied by an extraction of the molecular anions 0D-$[Sn_2Se_6]^{4-}$, confirms this suggestion: a set of $I-V$ characteristics, including $I-V$ hysteresis and chronoamperometry traces, demonstrate that both compounds are now conductive, with ionic conductivity dominating along both vertical and horizontal directions of $\mathbf{1}^{Cs}$ and $\mathbf{2}^{Cs}$. Notably, compound **1** not only turned into a conductive material $\mathbf{1}^{Cs}$, it additionally became slightly more conductive this way than $\mathbf{2}^{Cs}$. In summary, this work unravels the nonlinear conductive nature of selenido stannates and represents a step forward toward functional materials based on chalcogenido metalates.

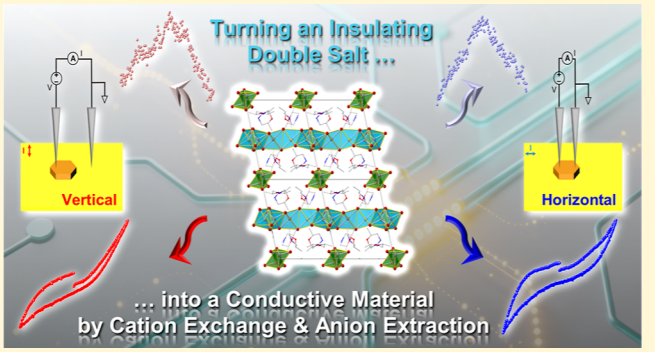

INTRODUCTION

Cluster-based chalcogenido metalates have shown application potential in photocatalysis[1−3] or electrocatalysis,[4,5] and as ionic conductors[6−10] owing to their electronic or ionic conducting properties combined with their porous characteristics.[11−13] However, their conductive nature has rarely been studied, although this would be an important step toward promoting their use as electron or ion conductors in electronics. For instance, the compound $(TMA)_2[FeGe_4Ch_{10}]$ (TMA = tetramethylammonium; Ch = S, Se) has been identified as a purely electronic conductor, whereas analogues in which Fe is replaced by M = Mn, Co, Ni, or Zn exhibit ion-electron-coupled conductivity.[11,14] As the anionic substructure in $(TMA)_2[MGe_4Ch_{10}]$ represents a three-dimensional network, the cations migrate diffusively within the channels and the electrons transport randomly along the framework.[11,14] In contrast, less has been known for compounds that consist of layer-like anionic substructures, which offers the possibility of investigating conductivity in both the vertical and horizontal directions on single crystals and this way understand the conductivity pathways much better. Potential future applications of such materials include memristors[15,16] or electrolyte-based flexible alkali-ion sensors for wearable sensors based on the change in ionic conductivity on the skin.[17−19]

For this, we synthesized model compounds based on the prominent 2D-$\{[Sn_3Se_7]^{2-}\}$ honeycomb-type substructure. One of them comprises counterions $(HDMMP)^+$ and $(C_3C_1Im)^+$ (HDMMP = protonated 2,6-dimethylmorpholine; C_3C_1Im = 1-propyl-3-methylimidazolium) between the anionic layers. Another compound comprises $(HDMMP)^+$ counterions only, and every second 2D-$\{[Sn_3Se_7]^{2-}\}$ layer is replaced with a layer of molecular 0D-$[Sn_2Se_6]^{4-}$ anions, which introduces an open circuit parallel to the 2D substructures. In addition, the compounds were treated with aqueous solution of CsCl to obtain cation-exchanged products. In case of the compounds with additional molecular anions, the latter were released into solution through this process. A full set of electrical measurements, including linear and cyclic current (I)−voltage

Received: May 14, 2026
Revised: July 16, 2026
Accepted: July 17, 2026

(V) sweeping, chronoamperometry trace, and temperature-dependent conductivity measurements, are performed to approach the conductive nature of selenido stannates using these four compounds.

RESULTS AND DISCUSSION

Scheme 1 illustrates the syntheses presented herein.

Scheme 1. Illustration of the Ionothermal Syntheses of Compounds 1 and 2[a]

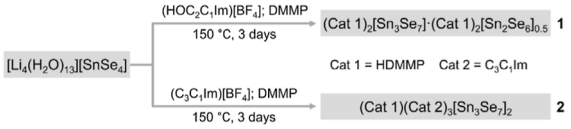

[a]Abbreviations are detailed in the text.

Treatment of $[Li_4(H_2O)_{13}][SnSe_4]$ in 1-hydroxyethyl-3-methyl-imidazolium tetrafluoroborate $(HOC_2C_1Im)[BF_4]$ and 2,6-dimethylmorpholine (DMMP) for 3 days at 150 °C afforded $(HDMMP)_2[Sn_3Se_7]\cdot(HDMMP)_2[Sn_2Se_6]_{0.5}$ (**1**) as air-stable single crystals (see the Supporting Information for more experimental details). Compound **1** crystallizes in the triclinic system, space group type $P\bar{1}$, with two formula units per unit cell (V = 2359.69(14) Å^3). It can be understood as a double-salt of half an equivalent of $(HDMMP)_4[Sn_2Se_6]$, comprising 0D-$[Sn_2Se_6]^{4-}$ anions, and $(HDMMP)_2[Sn_3Se_7]$, exhibiting the famous two-dimensional honeycomb-like (***hcb*** topology) substructure 2D-$\{[Sn_3Se_7]^{2-}\}$.[20−25] In the double salt, layers of 0D anions and 2D substructures, both oriented parallel to the crystallographic *ab* plane, alternate along the crystallographic *c* direction, with $(HDMMP)^+$ cations being embedded between the layers of selenido stannate anions (Figure 1a,c). By replacing the hydroxyl group in the ionic liquid cation with a methyl group, hence, using $(C_3C_1Im)[BF_4]$ instead of $(HOC_2C_1Im)[BF_4]$ as the reaction medium while keeping the other reaction conditions unchanged (see Supporting Information for details), we obtained air-stable single crystals of compound $(C_3C_1Im)_3(HDMMP)[Sn_3Se_7]_2$ (**2**). Compound **2** crystallizes in the monoclinic crystal system, space group type *Cc* with four formula units per unit cell (V = 5806.8(7) Å^3). This compound is based on exclusively the honeycomb-like (***hcb*** topology) 2D-$\{[Sn_3Se_7]^{2-}\}$ anionic substructure (Figure 1b,d), but here, we observe a mixed-cationic situation: the anionic layers are separated by both $(HDMMP)^+$ and $(C_3C_1Im)^+$ in a 1:3 ratio, while **1** bears $(HDMMP)^+$ counterions only. The Sn−Se bond lengths and Se−Sn−Se angles for **1** and **2** are found within the range of 2.4524(12)−2.7988(7) Å and 86.49(6)−127.22(7)°, respectively, in agreement with reported values of similar compounds.[26−28] The two compounds thus share structural similarities, but also differ in a way that makes them ideal candidates for comparison of further properties, which are

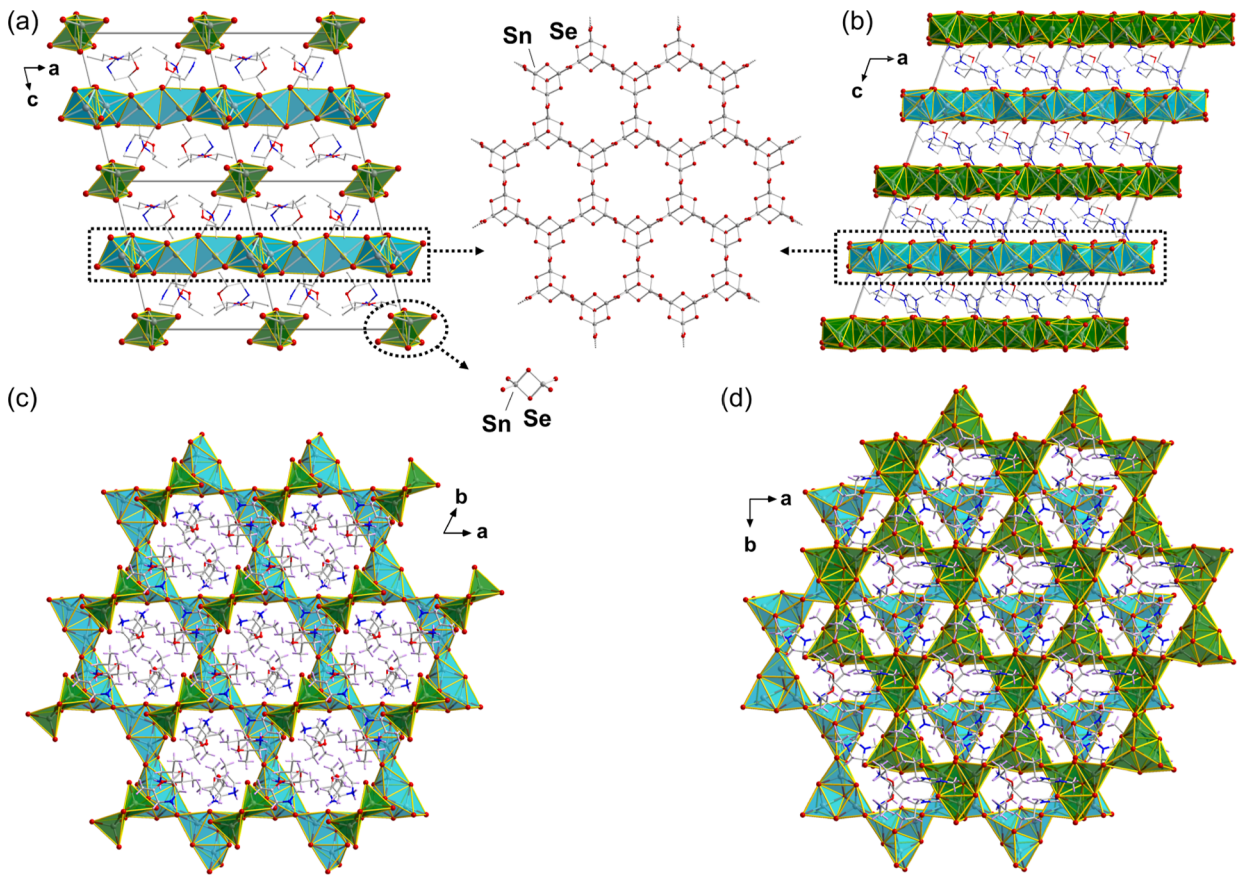

Figure 1. Comparison of the packing of anions and cations in the crystals of **1** (a,c) and **2** (b,d), viewed along the crystallographic *b* axis (a,b) or *c* axis (c,d). The 0D-$[Sn_2Se_6]^{4-}$ units and the 2D-$\{[Sn_3Se_7]^{2-}\}$ substructure are shown in polyhedral mode (left-hand and right-hand side) and are further detailed in ball-and-stick mode (center). Color code: Sn—gray, Se—wine red, C—light gray, N—blue, and O—red. Counterions are shown in wire mode, and H atoms are not shown for clarity.

https://doi.org/10.1021/acs.chemmater.6c01405
Chem. Mater. XXXX, XXX, XXX−XXX

discussed below. The two structures are illustrated in Figure 1 (see Figures S2–S5 for more structural details).

Micro-X-ray fluorescence (μ-XRF) investigations (Figures S6, S7 and Table S3) and powder X-ray diffraction (PXRD) measurements (Figures S8 and S9) served to verify the atomic ratio and phase purity. Solid-state diffuse-reflectance spectra (Figures S10 and S11) reveal that **1** and **2** are indirect optical band gap materials.[29]

The formation of **1** instead of **2** in the presence of 1-hydroxyethyl-3-methyl-imidazolium cations is attributed to the relatively protic nature of the hydroxyethyl groups on the $(HOC_2C_1Im)^+$ cations. They serve to effectively protonate DMMP molecules to form $(HDMMP)^+$ cations, which are included in the product, thereby replacing the originally present $(HOC_2C_1Im)^+$ cations and thus acting as an alternative structural template.

Salts comprising the 0D-$[Sn_2Ch_6]^{4-}$ anion, like $K_4[Sn_2Se_6]$,[30,31] are generally water-soluble, while known salts of the honeycomb-like substructure 2D-$\{[Sn_3Se_7]^{2-}\}$,[20−25] and also compounds **1** and **2**, are not. Additionally, organic cations in various chalcogenido metalates were shown to be replaced with Cs^+ by treatment with a concentrated aqueous solution of CsCl.[32] Given these two facts, we were interested to explore the effect of a cation exchange in these two related compounds on their solubility as well as their physical properties. We thus performed ion exchange experiments for **1** and **2** by suspension of single crystals in aqueous CsCl solution. This yielded two air-stable compounds, which we denominate as $\mathbf{1}^{Cs}$ and $\mathbf{2}^{Cs}$.

ESI mass spectra of the aqueous solutions obtained after the exchange reaction (Figures S12–S17) indicate an exchange and release of the counterion (for **1** and **2**) and the additional release of the 0D-$[Sn_2Se_6]^{4-}$ anion (in the case of compound **1**) into solution. The uniform distribution of Cs, Sn, and Se atoms within the solids, detected by energy-dispersive X-ray (EDX) elemental mapping analyses using scanning electron microscopy (SEM) coupled with μ-XRF measurements (Figures S19–S21 and Table S4) further demonstrate that cation exchange has occurred for both $\mathbf{1}^{Cs}$ and $\mathbf{2}^{Cs}$. Comparison of IR spectra of **1** and $\mathbf{1}^{Cs}$, as well as of **2** and $\mathbf{2}^{Cs}$ (Figures S22 and S23), still show the vibrational fingerprints of the organic cations, indicating that the exchange was not 100% complete. Comparison between the PXRD patterns of **1** and $\mathbf{1}^{Cs}$, as well as **2** and $\mathbf{2}^{Cs}$ (Figures S24 and S25) illustrate the anion-extraction and/or cation-exchange reactions.

To investigate, compare, and understand the conductive nature of these compounds, a set of electrical measurements was performed over a single crystal. As shown in Scheme 2, the hexagon-shaped crystals of **1**, $\mathbf{1}^{Cs}$, **2**, and $\mathbf{2}^{Cs}$ were placed horizontally on a gold-coated silicon wafer.

The $I-V$ characteristics were measured along vertical and horizontal directions of the crystals by varying the tungsten probes' positions as illustrated in the scheme: the vertical current flow, hence perpendicular to the crystallographic *ab* planes, is measured with one of the tungsten tips pointing to the top surface of the crystal and one to the gold substrate. By placing both tungsten probes on the crystal surface, the measured current flow crosses over the crystal in a horizontal direction. As outlined in the following, the measurements indicate that (a) we observe isotropic behavior of both compounds, (b) compound **1** exhibits insulating behavior, while compound **2** allows some current flow, and (c) electronic and ionic conduction collectively account for the nonlinear conductive nature of the compounds.

Scheme 2. Illustration of the Conductivity Measurement along Vertical and Horizontal Directions Over a Single Crystal of All Compounds

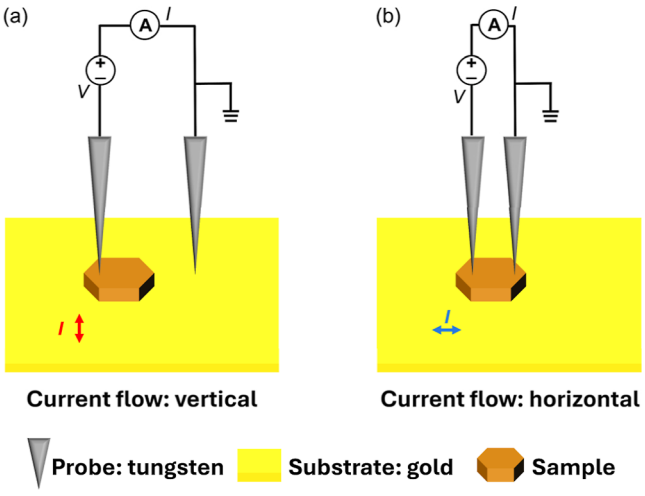

First, the $I-V$ characteristics were measured within an initial voltage sweep (−2 V → 2 V) over single crystals of the pristine compounds **1** and **2**. As shown in Figure 2a,b, the $I-V$ curves

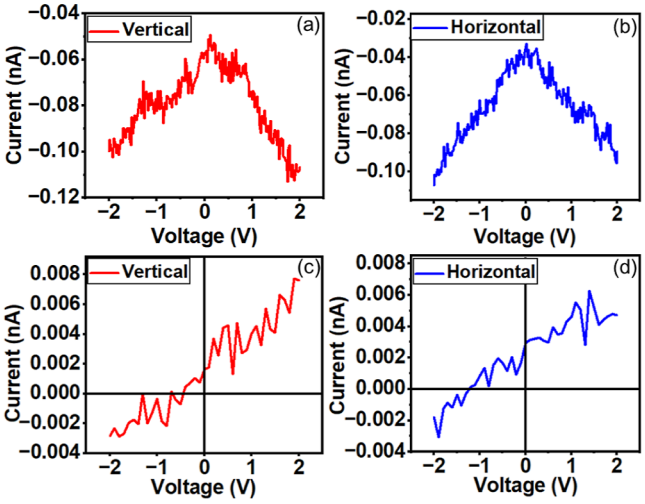

Figure 2. $I-V$ characteristics of compound **1** measured over a single crystal, along vertical (a) and horizontal directions (b), and of **2** along vertical (c) and horizontal directions (d).

measured along both vertical and horizontal directions of compound **1** resemble the pattern measured under open-circuit conditions (Figure S26), indicating its insulating behavior (hence, nearly no power was consumed by compound **1** according to $I-V$) within the voltage range under the measurement. However, for compound **2**, the measured $I-V$ characteristics within a voltage sweep (−2 V → 2 V) are nonlinear and asymmetric along both vertical and horizontal directions, revealing its semiconducting nature, although the measured currents are rather small even with a bias voltage at ±2 V (Figure 2c,d).

The difference in $I-V$ characteristics is assumed to be a result of the replacement of 2D-$\{[Sn_3Se_7]^{2-}\}$ substructures by the 0D-$[Sn_2Se_6]^{4-}$ units, leading to an open-circuit effect in **1**

https://doi.org/10.1021/acs.chemmater.6c01405
Chem. Mater. XXXX, XXX, XXX−XXX

regarding the horizontal setup. In the vertical direction, we see no electrical conductivity. Here, the higher negative charge density of the 0D units causes stronger electrostatic interactions between cations and anions, which reduces the mobility of the cations and, hence, their contribution to the overall conductivity that is measured.

Based on the structural features of the two compounds, which include open channels running through the crystals of compound **1** perpendicular to the *ab* plane, one would have expected compound **1** to be more (ion-)conductive. Given the higher mobility of alkali metal ions, *I*−*V* characteristics were thus recorded for a modified solid, in which the organic cations were replaced (to some extent) with Cs^+ cations. The choice of this cation was made as we assumed that the structures would remain least affected when using a larger cation to replace the organic molecules, hence allowing direct comparison. Indeed, upon ion exchange, we find this compound to be the more conductive one.

$\mathbf{1}^{Cs}$ was investigated by applying a voltage sweep from −2 to 2 V (denoted as forward sweeping) and from 2 V to −2 V (denoted as backward sweeping), see Figure 3.

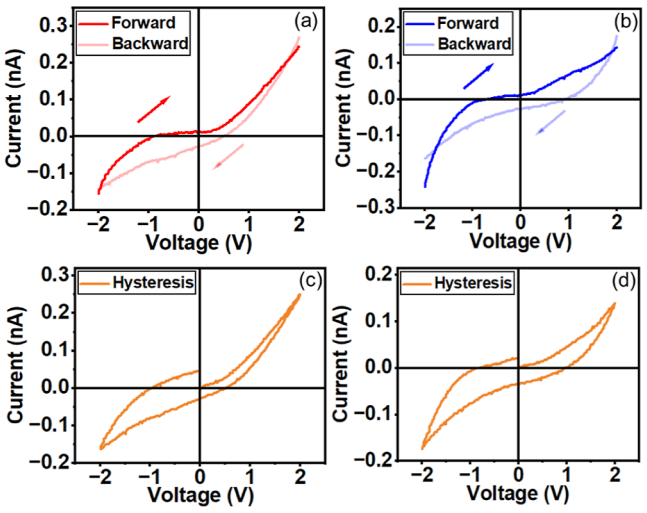

Figure 3. Forward (red and blue) and backward (pale-red and pale-blue) *I*−*V* curves of $\mathbf{1}^{Cs}$ measured along vertical (a) and horizontal (b) directions. *I*−*V* hysteresis of $\mathbf{1}^{Cs}$ measured over a consecutive voltage sweep (0 V → +2 V → −2 V → 0 V) along the vertical direction (c), and over the same consecutive voltage sweep order along the horizontal direction (d).

The *I*−*V* curves, measured along vertical and horizontal directions (Figure 3a,b), demonstrate that the voltage-dependent currents improve upon cation-exchange and anion-extraction of **1** to form $\mathbf{1}^{Cs}$. More importantly, the *I*−*V* curves feature nonzero-crossing current, indicating a capacitor-like *I*−*V* characteristic. To better understand the nonzero-crossing nature, the *I*−*V* hysteresis was investigated vertically and horizontally by applying a sweeping voltage order of 0 V → +2 V → −2 V → 0 V. Figure 3c displays the hysteresis measured along vertical direction of $\mathbf{1}^{Cs}$. At the initial stage while no bias voltage was applied, there is no current flow observed. As the voltage was swept from 0 V to +2 V, the current flow gradually increases. In the phase with a voltage sweeping from +2 V to −2 V, an open circuit voltage (V_{OC}) at +0.51 V is observed—at which the current is determined to be zero but with a voltage of 0.51 V applied. While decreasing the voltage from −2 to 0 V, a second V_{OC} at −0.98 V is obtained, indicating a pair of asymmetric V_{OC} along the vertical direction of $\mathbf{1}^{Cs}$. During the voltage sweep direction transition from +2 V to −2 V and −2 V to 0 V, two nonzero-crossing currents are observed at 0 V, suggesting the short circuit current (I_{SC}).[33] This is attributed to the existence of a displacement current (I_d), which is a sum of voltage change ($V\frac{dV}{dt}$) and capacitance change ($C\frac{dC}{dt}$) over time,[34] yet given that the former is a small number under quasi-static voltage sweeping mode, the latter dominates the change and leads to the observation of I_{SC} at 0 V, the two I_{SC} numbers are determined to be −0.029 and +0.048 nA. The horizontal *I*−*V* curve exhibits similar hysteresis phenomenon but with V_{OC} being +0.96 and −0.84 V, and I_{SC} being −0.035 and +0.021 nA (Figure 3d). In summary, the hysteresis suggests capacitor-like *I*−*V* characteristics observed in both vertical and horizontal directions for compound $\mathbf{1}^{Cs}$, yet with variations in the absolute V_{OC} and I_{SC} values. Comparison with the few available reports on conductivities of related chalcogenide-based compounds indicates that the values we measured are in the typical range (Table S5), and can now be optimized based on the insights we provide.[35,36]

The same phenomena were observed for $\mathbf{2}^{Cs}$, but with lower conductivity compared to $\mathbf{1}^{Cs}$ (see Supporting Information). The forward (voltage scans from −2 V to +2 V) and backward (voltage scans from +2 V to −2 V) current flows along the two directions display nonlinear characteristics, both exhibiting a pair of asymmetric V_{OC} and I_{SC} (Figure S27). The *I*−*V* hysteresis (Figure S28a) indicates the two V_{OC} are found at +0.89 and −1.01 V, respectively, and the two I_{SC}, measured as −0.016 and +0.018 nA, slightly differ from the V_{OC} and I_{SC} numbers observed from the *I*−*V* hysteresis along the vertical direction of $\mathbf{1}^{Cs}$. The horizontal *I*−*V* curve exhibits a similar hysteresis phenomenon, but with V_{OC} being +1.43 and −1.33 V, and I_{SC} being −0.007 and +0.01 nA (Figure S28b).

Chronoamperometry, as a tool for revealing conduction mechanisms of a material,[14] was performed over a single crystal of $\mathbf{1}^{Cs}$ along the two directions (Figure 4a,b). The current flows across vertical and horizontal directions of $\mathbf{1}^{Cs}$ were recorded while stepping the applied voltage by +0.5 V every 50 s between 0 and 5 V, according to the pattern depicted in Figure S29.

As illustrated in Figure 4a,b, at 0.0 to +1 V, the current flows are too small to be accurately distinguished from the noise floor. However, by applying higher voltage at +1.5 to +5.0 V, it was found that the current flows decrease gradually at a steady biased voltage, indicating an ionic conductivity along the vertical and horizontal directions. This behavior is attributed to the migration of Cs^+ cations through the six-membered channels of the anionic substructure in the vertical direction, and across the interlayer spacing of the two-dimensional networks in the horizontal direction.

For $\mathbf{2}^{Cs}$, the same phenomenon was observed from the chronoamperometry trace measured along the vertical direction (Figure S30a), indicating an ionic conductivity due to the movement of Cs^+ cations through the six-membered channels of the anionic network. However, the currents are too small to determine the conduction mechanisms along the horizontal direction (Figure S30b).

Finally, temperature-dependent *I*−*V* characteristics were carried out to demonstrate temperature effects on the conducting behaviors of $\mathbf{1}^{Cs}$ and $\mathbf{2}^{Cs}$. As depicted in Figures

https://doi.org/10.1021/acs.chemmater.6c01405
Chem. Mater. XXXX, XXX, XXX−XXX

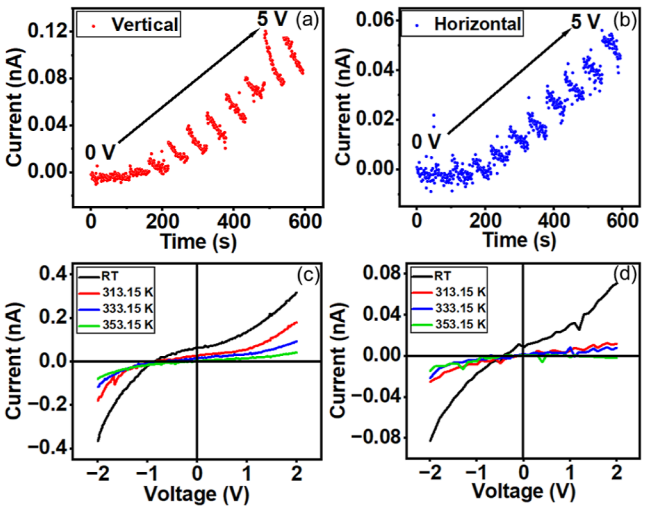

Figure 4. Chronoamperometry traces of $\mathbf{1}^{Cs}$ measured along vertical (a) and horizontal (b) directions, under applied voltages ranging from 0 V to +5 V, with steps of 0.5 V. Temperature-dependent $I-V$ curves of $\mathbf{1}^{Cs}$ measured along vertical (c) and horizontal (d) directions, $I-V$ curves measured along both directions were carried out at room temperature, 313.15, 333.15, and 353.15 K.

4c,d and S31, $I-V$ curves of $\mathbf{1}^{Cs}$ and $\mathbf{2}^{Cs}$ measured at four different temperatures (room temperature, 313.75, 333.75, and 353.75 K), show the conductivity unexpectedly drops with increasing temperature. We assume that an increased motion of the residual organic cations block the ion transport path of Cs^+ more effectively at higher temperatures, resulting in a nondirectional movement of Cs^+, and, consequently, reduced conductivity under these conditions. Interestingly, all temperature-dependent $I-V$ characteristics display temperature-dependent I_{SC} and temperature-independent V_{OC}. Additionally, temperature-dependent $I-V$ characteristics measured along the horizontal direction of $\mathbf{1}^{Cs}$ and $\mathbf{2}^{Cs}$ feature the same conduction behavior (Figures 4d and S31b), suggesting that ionic conductivity also dominates the overall conductivity along horizontal directions.

CONCLUSIONS

In conclusion, we have revealed the conductive nature of a series of selenido stannates, obtained from ionic liquids, and their cation-exchanged derivatives with a full set of $I-V$ measurements. The $I-V$ characteristics demonstrate that electronic and ionic conductivity govern the conductivity along vertical and horizontal directions of the 2D-$\{[Sn_3Se_7]^{2-}\}$-based compound **2**, respectively. Replacement of every second 2D-$\{[Sn_3Se_7]^{2-}\}$ substructure by a layer of 0D-$[Sn_2Se_6]^{4-}$ anions creates an open circuit situation, leading to insulating behavior of **1**. Upon a Cs^+-exchange process, however, the conductivities increase as confirmed by forward and backward $I-V$ curves, finally reaching reasonable values for this class of materials. This represents an excellent starting point for systematic optimization to follow.

Additionally, $I-V$ hystereses feature nonzero-crossing currents, suggesting capacitor-like characteristics along both directions for $\mathbf{1}^{Cs}$ and $\mathbf{2}^{Cs}$. Chronoamperometry traces show that Cs^+ migration dominates the conductivity from both horizontal and vertical directions of these compounds.

This work contributes to a fundamental understanding of the conductive nature of selenido stannates with organic versus inorganic cations, which will be intensified and transferred to other chalcogenido metalates in our future studies.

EXPERIMENTAL SECTION

General Synthesis Methods

All operations and reactions were performed in an argon atmosphere by using standard Schlenk line or glovebox techniques. $[Li_4(H_2O)_{13}][SnSe_4]$ was prepared according to the literature.[37] 2,6-Dimethylmorpholine (DMMP; Sigma-Aldrich, 99.8%) was dried over P_2O_5, distilled and stored over molecular sieve (3 Å); 1-propyl-3-methylimidazolium tetrafluoroborate, $(C_3C_1Im)[BF_4]$, from abcr GmbH (99%); 1-hydroethyl-3-methylimidazolium tetrafluoroborate, $(HOC_2C_1Im)[BF_4]$, from abcr GmbH (99%) were degassed before use. All reactions were carried out with ionothermal approaches, and the procedures for synthesizing compounds **1** and **2** are described in detail below.

Synthesis of $(HDMMP)_2[Sn_3Se_7]\cdot(HDMMP)_2[Sn_2Se_6]_{0.5}$ (1) (HDMMP = Protonated 2,6-Dimethylmorpholine)

30 mg of $[Li_4(H_2O)_{13}][SnSe_4]$ (0.065 mmol), 500 μL (2.337 mmol) of $(HOC_2C_1Im)[BF_4]$, and 100 μL (0.812 mmol) of DMMP were combined in a borosilicate glass ampule, which was flash-frozen in a liquid nitrogen dewar, evacuated to an internal pressure of 0.05 mbar, and subsequently flame-sealed. After being stood in a sand bowl for an hour, the sealed ampule was heated to 150 °C from room temperature at a heating rate of 30 °C/h, kept at 120 °C for 72 h, and then cooled down to room temperature at a cooling rate of 5 °C/h. Orange hexagonal crystals of **1** were obtained in a yield of approximately 69.7% (20 mg) with respect to $[Li_4(H_2O)_{13}][SnSe_4]$. Compound **1** is stable under ambient conditions for at least 1 day, but was stored in a glovebox for further use.

Synthesis of $(C_3C_1Im)_3(HDMMP)[Sn_3Se_7]_2$ (2)

30 mg of $[Li_4(H_2O)_{13}][SnSe_4]$ (0.065 mmol), 500 μL (2.358 mmol) of $(C_3C_1Im)[BF_4]$, and 100 μL (0.812 mmol) of DMMP were combined in a borosilicate glass ampule, which was flash-frozen in a liquid nitrogen dewar, evacuated to an internal pressure of 0.05 mbar, and subsequently flame-sealed. After being stood in a sand bowl for an hour, the sealed ampule was heated to 150 °C from room temperature at a heating rate of 30 °C/h, kept at 150 °C for 72 h, and then cooled down to room temperature at a cooling rate of 5 °C/h. Orange hexagonal crystals of **2** were obtained in a yield of approximately 71.9% (18 mg) with respect to $[Li_4(H_2O)_{13}][SnSe_4]$. Compound **2** is stable under ambient conditions for at least 1 day, but was stored in a glovebox for further use.

Light Microscopy

Light microscopic images of single crystals were obtained using the stereo light microscope SteREO Discovery.V8 by Carl Zeiss. The microscope was equipped with a high-intensive cold-light source CL 1500 ECO, an Achromat S 0.63× objective (FWD 107 mm), a PL 10×/21 Br ocular, and the microscope camera AxioCam MRc 5 with the camera adapter 60N-C 2/3″ 0.63×. The raw photo material was examined by the AxioVision40 × 64 4.9.1 SP1 software. The images are shown in Figure S1.

Single-Crystal X-ray Diffraction

The data for the X-ray structural analyses were collected at T = 100.0 K with Mo Kα-radiation (λ = 0.71073) on Bruker D8Quest diffractometer with a CMOS detector for compound **1**, and at T = 150.0 K with Cu Kα-radiation (λ = 1.54186 Å) on a Stoe STADI VARI diffractometer for compound **2**. The structures were solved by dual-space methods and refined by full matrix least-squares methods against F^2 using Olex-2,[38] and crystallographic data (excluding structure factors) for the structure reported in this paper have been deposited with the Cambridge Crystallographic Data Centre as supplementary publication nos. CCDC-2523694–CCDC-2523695. Copies of the data can be obtained free of charge on application to CCDC, 12 Union Road, Cambridge CB2 1EZ, UK [fax: (internat.) +44 1223/336-033; e-mail: deposit@ccdc.cam.ac.uk]. The crystal

https://doi.org/10.1021/acs.chemmater.6c01405
Chem. Mater. XXXX, XXX, XXX–XXX

data and refinement results are collected in Tables S1 and S2. Figures were created with Diamond 4.5.[39]

Micro-X-ray Fluorescence Spectroscopy

μ-XRF data were recorded on a Bruker M4 Tornado, equipped with an Rh-target X-ray tube and a silicon drift detector. The emitted fluorescence photons were detected with an acquisition time of 240 s as a point measurement. The spectra shown in Figures S6, S7 and Table S3 summarize the results of the measured Sn/Se ratio in comparison to that of the theoretical values.

Powder X-ray Diffraction

PXRD data were obtained with Cu Kα radiation in transmission mode on a Stoe StadiMP diffractometer using a Mythen2 detector system. The data were examined using WinXPOW.

Optical Absorption Spectroscopy

Optical properties of compounds **1** and **2** were measured under inert conditions employing a Varian Cary 5000 UV/vis/NIR spectrometer from Agilent, equipped with a Praying Mantis accessory for the solid-state samples. The spectra are shown in Figures S10, S11, and S18.

Ion-Exchange Experiments

The ion-exchange process was operated under Ar. As illustrated in Scheme S1, 10 mg of crystalline material of **1** or **2** was immersed in 10 mL of an aqueous solution of CsCl (0.5 M) in a Schlenk flask. The flask was heated to 75 °C and kept at this temperature for 24 h to allow the cation-exchange and anion-extraction process. After allowing the mixture to cool down to room temperature, the solution was filtered into another flask and analyzed by ESI-MS. The solid residue was washed three times with degassed water. The full process was repeated twice. The obtained solid samples were denoted as $\mathbf{1}^{Cs}$ and $\mathbf{2}^{Cs}$, respectively.

Electrospray Ionization Mass Spectrometry

ESI mass spectra were recorded with a Thermo Fisher Scientific Finnigan LTQ-FT spectrometer in positive and negative ion modes. The solutions obtained after filtering off $\mathbf{1}^{Cs}$ and $\mathbf{2}^{Cs}$ were analyzed by ESI-MS. The solutions were injected into the spectrometer with gastight 250 μL Hamilton syringes by syringe pump infusion. ESI(+) mass spectra are shown in Figures S12–S17.

Scanning Electron Microscopy

SEM images were collected using a Jeol JIB-4601F microscope.

EDX Spectroscopy

Elemental mapping images were measured using the EDX detector XFlash 5010 of Bruker Nano GmbH coupled with the scanning electron microscope Jeol JIB-4610F. Data acquisition was performed with an acceleration voltage of 15 kV and 5 min accumulation time. To determine the compositions, μ-XRF data were recorded as a point measurement on a single crystal for $\mathbf{1}^{Cs}$ and $\mathbf{2}^{Cs}$.

Infrared Spectroscopy

IR spectra were performed on a Nicolet iS50 Fourier-transform infrared (FTIR) spectrometer with attenuated total reflection. IR spectra are shown in Figures S22 and S23.

Conductivity Measurements

The $I-V$ curves were measured over single crystals of **1**, **2**, $\mathbf{1}^{Cs}$, and $\mathbf{2}^{Cs}$. All the measurements were performed by applying voltage to one of the tungsten probes while grounding the other, and the induced current was measured accordingly. All electrical measurements were performed with a Keithley Semiconductor Parameter Analyzer 4200. $I-V$ hysteresis was measured over a consecutive voltage sweep (0 V → +2 V → −2 V → 0 V) along both vertical and horizontal directions. The chronoamperometry traces were measured over single crystals, under applied voltages ranging from 0 V to +5 V, with steps of 0.5 V. Temperature-dependent $I-V$ curves were collected after heating the crystal up from room temperature to certain temperatures, including 313.15, 333.15, and 353.15 K. For comparison, the $I-V$ curve under open-circuit conditions was also provided.

■ ASSOCIATED CONTENT

Supporting Information

The Supporting Information is available free of charge at https://pubs.acs.org/doi/10.1021/acs.chemmater.6c01405.

Details on crystal photographs, X-ray diffraction analyses, μ-XRF spectroscopy, EDX measurements, PXRD patterns, ESI-mass spectrometry analyses, ion-exchange experiments, and conductivity measurements (PDF)

Accession Codes

Deposition Nos. 2523694–2523695 contain the supplementary crystallographic data for this paper. These data can be obtained free of charge via the joint Cambridge Crystallographic Data Centre (CCDC) and Fachinformationszentrum Karlsruhe Access Structures service.

■ AUTHOR INFORMATION

Corresponding Author

Stefanie Dehnen − *Institute of Nanotechnology (INT) and Karlsruhe Nano Micro Facility (KNMFi), Karlsruhe Institute of Technology (KIT), Karlsruhe 76131, Germany;* orcid.org/0000-0002-1325-9228; Email: stefanie.dehnen@kit.edu

Authors

Zhou Wu − *Institute of Nanotechnology (INT) and Karlsruhe Nano Micro Facility (KNMFi), Karlsruhe Institute of Technology (KIT), Karlsruhe 76131, Germany*

Hongrong Hu − *Institute of Nanotechnology (INT) and Karlsruhe Nano Micro Facility (KNMFi), Karlsruhe Institute of Technology (KIT), Karlsruhe 76131, Germany*

Bastian Weinert − *Institute of Nanotechnology (INT) and Karlsruhe Nano Micro Facility (KNMFi), Karlsruhe Institute of Technology (KIT), Karlsruhe 76131, Germany*

Jasmin Aghassi-Hagmann − *Institute of Nanotechnology (INT) and Karlsruhe Nano Micro Facility (KNMFi), Karlsruhe Institute of Technology (KIT), Karlsruhe 76131, Germany;* orcid.org/0000-0003-0348-041X

Complete contact information is available at: https://pubs.acs.org/10.1021/acs.chemmater.6c01405

Author Contributions

Z.W. and H.H. contributed equally to this work. The manuscript was written through the contributions of all authors.

Notes

The authors declare no competing financial interest.

■ ACKNOWLEDGMENTS

The work was financially supported by the German Research Foundation (Deutsche Forschungsgemeinschaft, DFG) under Germany's Excellence Strategy − 2082/2 − 390761711. Z.W. acknowledges a Ph.D. fellowship by the China Scholarship Council (CSC No. 202006920030).

■ ABBREVIATIONS

TMA	tetramethylammonium
DMMP	2,6-dimethylmorpholine
HOC_2C_1Im	1-hydroxyethyl-3-methyl-imidazolium
C_3C_1Im	1-propyl-3-methyl-imidazolium

μ-XRF	micro-X-ray fluorescence
ESI	electrospray ionization
IR	infrared spectroscopy
PXRD	powder X-ray diffraction

REFERENCES

(1) Liu, D.; Liu, Y.; Huang, P.; Zhu, C.; Kang, Z.; Shu, J.; Chen, M.; Zhu, X.; Guo, J.; Zhuge, L.; Bu, X.; Feng, P.; Wu, T. Highly Tunable Heterojunctions from Multimetallic Sulfide Nanoparticles and Silver Nanowires. *Angew. Chem., Int. Ed.* **2018**, *57* (19), 5374−5378.

(2) Li, Z.-Q.; Mo, C.-J.; Guo, Y.; Xu, N.-N.; Zhu, Q.-Y.; Dai, J. Discrete Supertetrahedral CuInS Nanoclusters and Their Application in Fabrication of Cluster-Sensitized TiO_2 Photoelectrodes. *J. Mater. Chem. A* **2017**, *5* (18), 8519−8525.

(3) Benkada, A.; Reinsch, H.; Poschmann, M.; Krahmer, J.; Pienack, N.; Bensch, W. Synthesis and Characterization of a Rare Transition-Metal Oxothiostannate and Investigation of Its Photocatalytic Properties. *Inorg. Chem.* **2019**, *58* (4), 2354−2362.

(4) Liu, D.; Fan, X.; Wang, X.; Hu, D.; Xue, C.; Liu, Y.; Wang, Y.; Zhu, X.; Guo, J.; Lin, H.; Li, Y.; Zhong, J.; Li, D.; Bu, X.; Feng, P.; Wu, T. Cooperativity by Multi-Metals Confined in Supertetrahedral Sulfide Nanoclusters to Enhance Electrocatalytic Hydrogen Evolution. *Chem. Mater.* **2019**, *31* (2), 553−559.

(5) Wang, X.; Wang, X.-L.; Lv, J.; Wu, Z.; Zhang, J.; Hu, D.; Xue, C.; Li, D.; Zhu, X.; Wu, T. 0D/1D Heterostructure for Efficient Electrocatalytic CO_2-to-C1 Conversion by Ultra-Small Cluster-Based Multi-Metallic Sulfide Nanoparticles and MWCNTs. *Chem. Eng. J.* **2021**, *422*, 130045.

(6) Zhou, L.; Bazak, J. D.; Singh, B.; Li, C.; Assoud, A.; Washton, N. M.; Murugesan, V.; Nazar, L. F. A New Sodium Thioborate Fast Ion Conductor: $Na_3B_5S_9$. *Angew. Chem., Int. Ed.* **2023**, *62* (30), No. e202300404.

(7) Kaup, K.; Assoud, A.; Liu, J.; Nazar, L. F. Fast Li-Ion Conductivity in Superadamantanoid Lithium Thioborate Halides. *Angew. Chem., Int. Ed.* **2021**, *60* (13), 6975−6980.

(8) Duchardt, M.; Haddadpour, S.; Kaib, T.; Bron, P.; Roling, B.; Dehnen, S. Different Chemical Environments of $[Ge_4Se_{10}]^{4-}$ in the Li^+ Compounds $[Li_4(H_2O)_{16}][Ge_4Se_{10}]\cdot_{4.33}H_2O$, $[\{Li_4(Thf)_{12}\}$-$Ge_4Se_{10}]$, and $[Li_2(H_2O)_8][MnGe_4Se_{10}]$, and Ionic Conductivity of Underlying "$Li_4Ge_4Se_{10}$". *Inorg. Chem.* **2021**, *60* (7), 5224−5231.

(9) Holmes, S. E.; Kondek, J.; Zhang, P.; Faka, V.; Newnham, J. A.; Gronych, L. M.; Hansen, M. R.; Zeier, W. G.; Cui, Y. LiI-Modified Glass-Ceramic Lithium Thioborate: From Fundamentals to Applications in Solid-State Batteries. *Chem. Mater.* **2025**, *37* (7), 2642−2649.

(10) Ma, Y.; Wan, J.; Xu, X.; Sendek, A. D.; Holmes, S. E.; Ransom, B.; Jiang, Z.; Zhang, P.; Xiao, X.; Zhang, W.; Xu, R.; Liu, F.; Ye, Y.; Kaeli, E.; Reed, E. J.; Chueh, W. C.; Cui, Y. Experimental Discovery of a Fast and Stable Lithium Thioborate Solid Electrolyte, $Li_{6+2x}[B_{10}S_{18}]$-S_x ($x \approx 1$). *ACS Energy Lett.* **2023**, *8* (6), 2762−2771.

(11) McKenzie, J.; Le, K. N.; Bardgett, D. J.; Collins, K. A.; Ericson, T.; Wojnar, M. K.; Chouinard, J.; Golledge, S.; Cozzolino, A. F.; Johnson, D. C.; Hendon, C. H.; Brozek, C. K. Conductivity in Open-Framework Chalcogenides Tuned via Band Engineering and Redox Chemistry. *Chem. Mater.* **2022**, *34* (4), 1905−1920.

(12) Zheng, N.; Bu, X.; Feng, P. Synthetic Design of Crystalline Inorganic Chalcogenides Exhibiting Fast-Ion Conductivity. *Nature* **2003**, *426* (6965), 428−432.

(13) Zheng, N.; Bu, X.; Wang, B.; Feng, P. Microporous and Photoluminescent Chalcogenide Zeolite Analogs. *Science* **2002**, *298* (5602), 2366−2369.

(14) McKenzie, J.; Kempler, P. A.; Brozek, C. K. Solvent-Controlled Ion-Coupled Charge Transport in Microporous Metal Chalcogenides. *Chem. Sci.* **2022**, *13* (43), 12747−12759.

(15) Campbell, K. A. Self-directed channel memristor for high temperature operation. *Microelectron. J.* **2017**, *59*, 10−14.

(16) Sarwat, S. G.; Moraitis, T.; Wright, C. D.; Bhaskaran, H. Chalcogenide optomemristors for multi-factor neuromorphic computation. *Nat. Commun.* **2022**, *13*, 2247.

(17) Li, Y.; Bai, N.; Chang, Y.; Liu, Z.; Liu, J.; Li, X.; Yang, W.; Niu, H.; Wang, W.; Wang, L.; Zhu, W.; Chen, D.; Pan, T.; Guo, C. F.; Shen, G. Flexible Iontronic Sensing. *Chem. Soc. Rev.* **2025**, *54*, 4651−4700.

(18) Wang, J.; Wei, X.; Shi, J.; Bai, N.; Wan, X.; Li, B.; Chen, Y.; Jiang, Z.; Guo, C. F. High-resolution Flexible Iontronic Skins for Both Negative and Positive Pressure Measurement in Room Temperature Wind Tunnel Applications. *Nat. Commun.* **2024**, *15*, 7094.

(19) Chen, X.; Xia, X.; Guo, C. F. Flexible Iontronic Sensing: Ionic Materials, Electrodes, and Encapsulation. *Adv. Funct. Mater.* **2026**, *36*, No. e12920.

(20) Santner, S.; Sprenger, J. A. P.; Finze, M.; Dehnen, S. The Role of $[BF_4]^-$ and $[B(CN)_4]^-$ Anions in the Ionothermal Synthesis of Chalcogenidometalates. *Chem.—Eur. J.* **2018**, *24* (14), 3474−3480.

(21) Santner, S.; Dehnen, S. $[M_4Sn_4Se_{17}]^{10-}$ Cluster Anions (M = Mn, Zn, Cd) in a Cs^+ Environment and as Ternary Precursors for Ionothermal Treatment. *Inorg. Chem.* **2015**, *54* (4), 1188−1190.

(22) Xiong, W.-W.; Miao, J.; Ye, K.; Wang, Y.; Liu, B.; Zhang, Q. Threading Chalcogenide Layers with Polymer Chains. *Angew. Chem., Int. Ed.* **2015**, *54* (2), 546−550.

(23) Wang, K.-Y.; Liu, H.-W.; Zhang, S.; Ding, D.; Cheng, L.; Wang, C. Selenidostannates and a Silver Selenidostannate Synthesized in Deep Eutectic Solvents: Crystal Structures and Thermochromic Study. *Inorg. Chem.* **2019**, *58* (5), 2942−2953.

(24) Xue, C.; Li, R.; Chen, W.; Zhang, Y.; Zhang, N.; Qu, K.; Li, R.; Yang, H. Subtly Regulating Layered Tin Chalcogenide Frameworks for Optimized Photo-Induced Carrier Separation. *Inorg. Chem. Front.* **2023**, *10* (22), 6588−6595.

(25) Qi, X.-H.; Du, K.-Z.; Feng, M.-L.; Gao, Y.-J.; Huang, X.-Y.; Kanatzidis, M. G. Layered $A_2Sn_3S_7\cdot 1.25H_2O$ (A = Organic Cation) as Efficient Ion-Exchanger for Rare Earth Element Recovery. *J. Am. Chem. Soc.* **2017**, *139* (12), 4314−4317.

(26) Ruzin, E.; Zent, E.; Matern, E.; Massa, W.; Dehnen, S. Syntheses, Structures, and Comprehensive NMR Spectroscopic Investigations of Hetero-Chalcogenidometallates: The Right Mix toward Multinary Complexes. *Chem.—Eur. J.* **2009**, *15* (21), 5230−5244.

(27) Lu, J.; Shen, Y.; Wang, F.; Tang, C.; Zhang, Y.; Jia, D. Solvothermal Syntheses and Characterizations of Selenidostannate Salts of Transition Metal Complex Cations: Conformational Flexibility of the Lamellar $[Sn_3Se_7]^{2n-}$ Anion. *Z. Anorg. Allg. Chem.* **2015**, *641* (3−4), 561−567.

(28) Lin, Q.; Bu, X.; Feng, P. An Infinite Square Lattice of Super-Supertetrahedral T6-like Tin Oxyselenide Clusters. *Chem. Commun.* **2014**, *50* (31), 4044−4046.

(29) Makuła, P.; Pacia, M.; Macyk, W. How to Correctly Determine the Band Gap Energy of Modified Semiconductor Photocatalysts Based on UV−Vis Spectra. *J. Phys. Chem. Lett.* **2018**, *9* (23), 6814−6817.

(30) Haddadpour, S.; Melullis, M.; Staesche, H.; Mariappan, C. R.; Roling, B.; Clérac, R.; Dehnen, S. Inorganic Frameworks from Selenidotetrelate Anions $[T_2Se_6]^{4-}$ (T = Ge, Sn): Synthesis, Structures, and Ionic Conductivity of $[K_2(H_2O)_3][MnGe_4Se_{10}]$ and $(NMe_4)_2[MSn_4Se_{10}]$ (M = Mn, Fe). *Inorg. Chem.* **2009**, *48* (4), 1689−1698.

(31) Eisenmann, B.; Hansa, J. Crystal Structure of Tetrapotassium Hexaselenodistannate, $K_4Sn_2Se_6$. *Z. Kristallogr. Cryst. Mater.* **1993**, *203* (1−2), 299−300.

(32) Yang, H.; Luo, M.; Luo, L.; Wang, H.; Hu, D.; Lin, J.; Wang, X.; Wang, Y.; Wang, S.; Bu, X.; Feng, P.; Wu, T. Highly Selective and Rapid Uptake of Radionuclide Cesium Based on Robust Zeolitic Chalcogenide via Stepwise Ion-Exchange Strategy. *Chem. Mater.* **2016**, *28* (23), 8774−8780.

(33) Zhu, S.; Zhou, G.; Yuan, W.; Mao, S.; Yang, F.; Fu, G.; Sun, B. Non-Zero-Crossing Current-Voltage Hysteresis Behavior Induced by Capacitive Effects in Bio-Memristor. *J. Colloid Interface Sci.* **2020**, *560*, 565−571.

(34) Zheng, L.; Sun, B.; Chen, Y.; Li, T.; Mao, S.; Zhu, S.; Wang, H.; Zhang, Y.; Lei, M.; Zhao, Y. The Redox of Hydroxyl-Assisted Metallic

Filament Induced Resistive Switching Memory Based on a Biomaterial-Constructed Sustainable and Environment-Friendly Device. *Mater. Today Chem.* **2018**, *10*, 167−174.
(35) Hatz, A.-K.; Moudrakovski, I.; Bette, S.; Terban, M. W.; Etter, M.; Joos, M.; Vargas-Barbosa, N. M.; Dinnebier, R. E.; Lotsch, B. V. Fast Water-Assisted Lithium Ion Conduction in Restacked Lithium Tin Sulfide Nanosheets. *Chem. Mater.* **2021**, *33*, 7337−7349.
(36) Lungu, I.; Patru, R. E.; Galca, A. C.; Pintilie, L.; Potlog, T. DC current−voltage and impedance spectroscopy characterization of *n*CdS/*p*ZnTe HJ. *Sci. Rep.* **2024**, *14*, 12955.
(37) Kaib, T.; Bron, P.; Haddadpour, S.; Mayrhofer, L.; Pastewka, L.; Järvi, T. T.; Moseler, M.; Roling, B.; Dehnen, S. Lithium Chalcogenidotetrelates: LiChT—Synthesis and Characterization of New Li^+ Ion Conducting Li/Sn/Se Compounds. *Chem. Mater.* **2013**, *25* (15), 2961−2969.
(38) Sheldrick, G. M. Crystal Structure Refinement with *SHELXL*. *Acta Crystallogr., Sect. C: Struct. Chem.* **2015**, *71*, 3−8.
(39) Putz, K.; Brandenburg, K. *Diamond—Crystal and Molecular Structure Visualization*, Crystal Impact; GbR: Kreuzherrenstr., Bonn, Germany, 2025, Vol. *102*, p 53227.

https://doi.org/10.1021/acs.chemmater.6c01405
Chem. Mater. XXXX, XXX, XXX−XXX